Industrial Chemistry & Materials

ROYAL SOCIETY OF CHEMISTRY

PAPER

View Article Online
View Journal

Cite this: DOI: 10.1039/d5im00302d

Highly conjugated 2D COF/MOF composites for bifunctional electrocatalytic alkaline HER and OER with enhanced activity and stability

Yang Liu,[ab] Zhao-Di Yang,*[a] Rui Zhang,[a] Yingchao Lai,[a] Yu Zhang*[b] and Guiling Zhang[a]

Electrocatalytic water splitting, consisting of the anodic oxygen evolution reaction (OER) and cathodic hydrogen evolution reaction (HER), represents a promising renewable energy technology for producing ultra-high purity hydrogen through efficient energy conversion and storage. However, the practical implementation of this technology in an alkaline environment is hindered by the sluggish kinetics of both the HER and OER, which significantly limit the water splitting efficiency. Thus, the development of highly active and stable alkaline HER/OER electrocatalysts is urgently needed but remains challenging. In this work, we synthesized a novel two-dimensional (2D) highly conjugated COF/MOF composite (COF-C_4N/THQ-M) through a post-synthesis method. This method enables the controlled growth of a part of COF-C_4N at the edges of THQ-M MOF to prevent the structural disintegration of THQ-M, consequently enhancing the surface charge transfer efficiency and further improving the catalytic activity and stability of the composite. By regulating the metal sites, COF-C_4N/THQ-Co and COF-C_4N/THQ-Co_2Fe_1 are proposed to be the optimal alkaline HER electrocatalysts with an overpotential of 58 mV at –10 mA cm^{-2} and the alkaline OER electrocatalysts with 314 mV at 10 mA cm^{-2}, respectively, which are superior to most of the reported non-precious metal electrocatalysts. The charge transfer characteristics and the alkaline HER and OER pathways were calculated based on DFT calculations to reveal the synergistic mechanism between COF-C_4N and THQ-M. This work provides a novel idea for developing high-performance bifunctional electrocatalysts for alkaline water splitting applications based on hybrid highly conjugated COF/MOF systems.

Keywords: Two-dimensional covalent organic framework; Metal–organic framework; COF/MOF composite; Electrocatalytic oxygen evolution reaction; Electrocatalytic hydrogen evolution reaction.

Received 19th October 2025,
Accepted 31st December 2025

DOI: 10.1039/d5im00302d

rsc.li/icm

1 Introduction

Hydrogen energy, as an environmentally friendly fuel with a high energy density and non-polluting combustion products, is regarded as an ideal energy resource to replace fossil fuels.[1–3] Electrocatalytic water splitting, consisting of the anodic OER and cathodic HER, is a promising renewable energy conversion and storage technology to produce ultra-high purity hydrogen, which has attracted much attention.[4–7] The OER process requires a complex multi-step electron/proton reaction, and its slow kinetics constrains the overall performance of electrochemical energy conversion devices.[8] Electrocatalytic alkaline HER has also been extensively studied due to its favorable reaction kinetics for water splitting, which is the cathode half-reaction.[9–11] However, the kinetic steps of the HER under alkaline conditions are relatively more complicated than the acidic HER.[12] In the alkaline HER process, the dissociation of water provides a source of protons, and the breaking of the OH–H bond of the water molecule introduces additional energy barriers that greatly hinder the alkaline HER reaction rate.[13,14] Even the HER rate on Pt catalysts in alkaline media is several orders of magnitude lower than in acidic media.[15] Therefore, the splitting of water molecules needs to be promoted to accelerate the slow kinetics of the alkaline HER. It was shown that the adsorption and desorption of water during the electrocatalytic alkaline HER correspond exactly to the adsorption and desorption of hydroxyl groups, respectively.[16,17] The stronger OH binding ability of catalysts facilitates the polarization of water molecules and lengthens the OH–H bond, thus greatly facilitating water splitting.[18,19]

[a] Heilongjiang Provincial Key Laboratory of CO_2 Resource Utilization and Energy Catalytic Materials, School of Materials Science and Chemical Engineering, Harbin University of Science and Technology, Harbin, Heilongjiang, 150080, China. E-mail: yangzhaodi@163.com
[b] Institute of Process Engineering, Chinese Academy of Sciences, Beijing, 100080, China. E-mail: zhangyu@ipe.ac.cn

Currently, the employed OER and HER electrocatalysts are still noble metal Ir/Ru-based and Pt-based materials, but their high cost and scarce resources limit their large-scale applications.[20,21] It was found that transition metal iron-, cobalt-, and nickel-based materials[22] exhibit excellent OER catalytic activities in alkaline media. The low-coordinated metal sites on the surface of these compounds are suitable for the chemisorption and dissociation of the intermediates (OH* and OOH*), which are essential for alkaline HER and OER, respectively. However, it remains challenging to explore highly active and stable OER and HER electrocatalysts in alkaline media.

MOFs have attracted increasing attention due to their high specific surface area, homogeneous pore size distribution, and diverse structures,[23] and have had a wide range of applications.[24,25] In recent years, MOFs with high catalytic activity have been designed and constructed in the field of catalysis by selecting different metal centers and specific organic ligands. They have been widely applied in different types of electrocatalytic reactions, such as HER, hydrogen oxidation reaction (HOR), oxygen reduction reaction (ORR), and OER.[26–29] However, most MOFs exhibit poor electrical conductivity, low intrinsic activity, and limited mass transfer due to their microporous structures.[30] The MX_4 family (M is a transition metal; X = NH, O, S) is commonly applied to build 2D semiconductive MOF materials. The orbital interactions can be significantly modulated by changing the metal and the coordinating atoms (X), thus effectively tuning the electronic structures of the framework.[31–33] Most of the reported MX_4 MOFs are coordinated to metals *via* NH or S, whereas extending the coordinating atoms to oxygen analogs is synthetically challenging. In 2018, Bao *et al.* utilized a Cu(II) salt and tetrahydroxy-1,4-quinone (THQ) to generate a highly conjugated conductive 2D MOF ($Cu_3(C_6O_6)_2$), which possessed high conductivity.[34] In 2020, Chen *et al.* synthesized a redox-active 2D copper-benzoquinone (Cu-THQ) MOF using a simple solvothermal method, which exhibited good electrochemical activity, high reversible capacity, and good cycling stability.[35] These studies on the structure–property relationship of MOF materials provide new opportunities for electronics, sensing, and energy-related applications.

Furthermore, the electrocatalytic performance of MOFs was enhanced by applying the strategy of forming composites with other catalytically active materials. Zeng *et al.* reported the synthesis of core–shell Co-COF and MIL-88A-MOF-based composite catalysts for OER. The synergistic interaction between the COF-shell and MOF-core resulted in higher catalytic activity than the single COF and MOF.[36] Xu *et al.* similarly designed COF and MOF heterostructures and realized core–shell structure carbon frameworks *via* the direct pyrolysis of TP-BPY-COF@ZIP-67.[37] The COF shell layer prevented the collapse and aggregation of ZIF-67 and improved its electrical conductivity, realizing a bifunctional ORR and HER catalytic performance. These works provide ideas for the design and preparation of novel COF/MOF composite electrocatalysts. The current methods for preparing COF/MOF composites include direct condensation, post-synthesis modification, *in situ* synthesis, and π–π stacking.[38–40] Li *et al.* achieved a highly matching COF/MOF-5 composite through a "plug-socket anchoring" strategy. After grafting $-NH_2$ on the surface of MOF-5, a homogeneous and stable COF shell was constructed, while maintaining the crystallinity of MOF.[41] Co-COF@MOF was obtained by growing TP-BPY-COF on the surface of MIL-88A-MOF *via* an *in situ* strategy utilizing the bipyridine unit in the COF shell to anchor the Co ions. This catalyst exhibited only OER activity (overpotential of 328 mV in 1 M KOH).[36] Most COF/MOF composites are prepared by introducing MOFs containing $-NH_2$ groups on their surface during the synthesis of COFs *via* Schiff base reaction. However, the limited number of MOFs containing $-NH_2$ groups or are capable of undergoing amino-functionalization hinders the preparation of MOF and COF composites. Gao *et al.* constructed structurally stable core–shell MOF@COF composites *via* π–π stacking interactions.[42] Employing PCN-222-Co as the core, *p*-phenylenediamine (Pa) was homogeneously dispersed on its surface by ultrasonication, and then 1,3,5-tricarbonylresorcinol (Tp) was added to react with Pa to prepare the shell of COF. However, COF/MOF composites prepared *via* π–π stacking interactions also exhibit some drawbacks, such as uneven distribution of COF on the surface of MOF. Consequently, although currently, COF/MOF composite electrocatalysts have made initial progress in some fields, those with simultaneous bifunctional OER/HER activity under alkaline conditions are still relatively scarce and need to be further investigated and improved.

In 2019, our group successfully synthesized COF-C_4N *via* the solvothermal reaction of 2,3,6,7,10,11-triphenylenehexamine hexahydrochloride (TPHA) and hexaketocyclohexane octahydrate (HKH). The synthesized highly conjugated COF-C_4N displayed moderate OER activity (overpotential of 349 mV at 10 mA cm^{-2}).[43] Its good crystallinity and conductivity, as well as high stability under alkaline conditions, are the main reasons for its OER performance. In this work, we designed a novel highly conjugated 2D COF/MOF composite by synthesizing COF-C_4N using THQ-M as the substrate (M = Co, Fe, and bimetallic Co_xFe_y) *via* a post-synthesis strategy, and it was observed that COF-C_4N/THQ-M displayed bifunctional catalytic activity in alkaline HER/OER and has higher catalytic activity for HER/OER than single THQ-M and COF-C_4N. The HER and OER overpotentials of COF-C_4N/THQ-Co in alkaline media were 58 mV (@ −10 mA cm^{-2}) and 339 mV (@ 10 mA cm^{-2}), respectively, which are superior to that of most non-precious metal catalysts. COF-C_4N/THQ-Co_2Fe_1 also shows good bifunctional HER/OER activity, with HER and OER overpotentials of 132 mV (@ −10 mA cm^{-2}) and 314 mV (@ 10 mA cm^{-2}). Density functional theory (DFT) calculations were carried out to reveal the synergistic mechanism in the catalytic reaction pathways and charge transfer for HER and OER.

2 Results and discussion

2.1 Characterization of structures and morphologies

The COF-C_4N/THQ-Co composite catalyst was synthesized as depicted in Fig. 1a. THQ-Co was prepared *via* hydrothermal reaction using THQ and $CoCl_2{\cdot}6H_2O$ at 85 °C for 12 h.[44,45] Then, the COF-C_4N/THQ-Co composite was obtained by placing TPHA and HKH in a Schlenk tube containing THQ-Co *via* the solvothermal method. In addition, we also prepared THQ-M (M = Fe, Ni, Cu) as well as bimetallic THQ-Co_1Fe_2 and THQ-Co_2Fe_1 MOF materials, and then mono/bimetallic COF-C_4N/THQ-M composites.

The crystalline structures of the synthesized COF-C_4N, THQ-M, and COF-C_4N/THQ-M composites were characterized using powder X-ray diffraction (PXRD) measurements combined with simulation. As shown in Fig. 1b and S1, the AA stacking pattern of THQ-Co matches well with the experimental results, and THQ-Co showed diffraction peaks

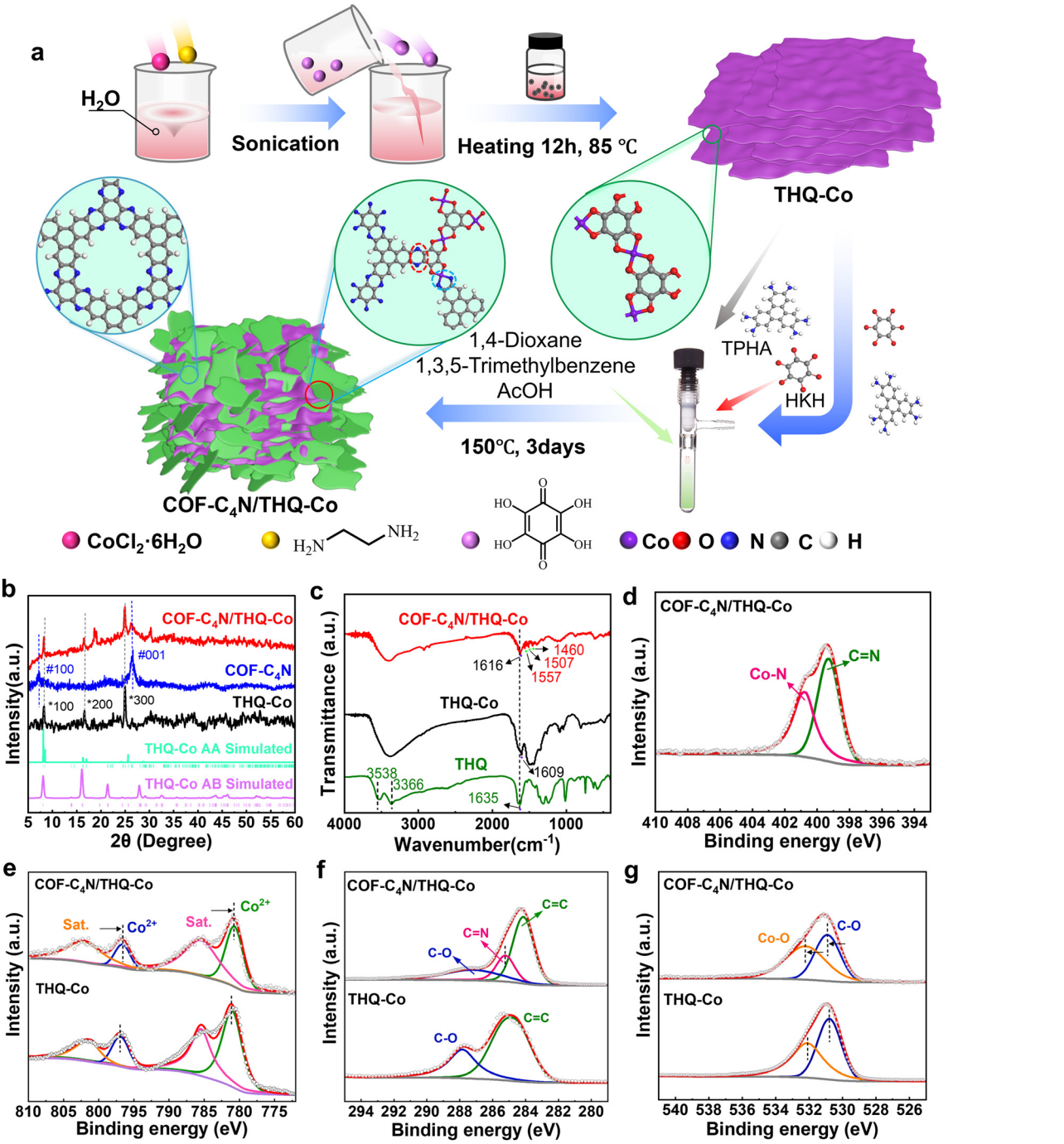

Fig. 1 (a) Schematic of the procedure for the synthesis of the COF-C_4N/THQ-Co composite catalysts; (b) PXRD patterns; (c) FT-IR spectra; (d) N 1s spectra of COF-C_4N/THQ-Co; and (e) Co 2p, (f) C 1s, and (g) O 1s spectra of THQ-Co and COF-C_4N/THQ-Co.

at 8.23°, 16.62°, and 24.99°, corresponding to the (100), (200), and (300) lattice planes, respectively. By altering the metal, the THQ-Fe, THQ-Cu, and THQ-Ni samples were prepared. The measured XRD patterns of THQ-Fe, THQ-Cu and THQ-Ni also showed their good crystallinity, indicating their suitable preparation methods and reaction conditions (Fig. S1).[46] The peaks of the COF-C_4N at 2θ = 7.1° and 26.6° correspond to the (100) and (001) lattice planes, respectively (Fig. 1b, blue curve).[43] The XRD pattern of the COF-C_4N/THQ-Co composite showed that the interaction between the two materials reduces the lattice order in the composite sample. This results in weakened XRD characteristic peak intensities and decreased crystallinity. However, its XRD pattern showed all the characteristic peaks of THQ-Co and the peak at 26.6° corresponding to the (001) lattice plane of COF-C_4N, indicating that the crystalline structure of THQ-Co was well preserved (Fig. 1b, red curve) and COF-C_4N maintained a good interlayer structure.

The Fourier transform infrared (FT-IR) spectra of the TPHA, HKH, THQ, THQ-M (M = Co, Fe, Ni, Cu), bimetallic THQ-Co_1Fe_2, THQ-Co_2Fe_1, and COF-C_4N/THQ-M composite samples are shown in Fig. 1c and S2 and S3. Compared to THQ, the OH peaks at 3538 cm^{-1} and 3366 cm^{-1} disappeared in the FT-IR spectrum of THQ-Co. The C═O absorption peak at 1635 cm^{-1} in the spectrum of THQ (Fig. 1c, green curve) shifted toward a lower wavenumber (1609 cm^{-1}), which confirmed the efficient coordination between Co and O (Fig. 1c, black curve). In the FT-IR spectrum of COF-C_4N/THQ-Co, all the peaks for THQ-Co were still present, where the C═O absorption peak blue-shifted to 1616 cm^{-1}, while new peaks appeared at 1560 cm^{-1}, 1508 cm^{-1}, and 1458 cm^{-1}, corresponding to the characteristic peaks of the phenazine bond (Fig. 1c, red curve). The FT-IR spectra of the other THQ-M (M = Fe, Ni, Cu), bimetallic THQ-Co_1Fe_2, THQ-Co_2Fe_1, and COF-C_4N/THQ-M composite samples likewise demonstrate their successful preparation.

The chemical and electronic states of the catalysts were analyzed by X-ray photoelectron spectroscopy (XPS). The XPS spectra revealed the presence of five elements, C, N, O, Co, and Cl, in COF-C_4N/THQ-Co (Fig. S4a). The N 1s spectrum of the COF-C_4N/THQ-Co sample exhibits two characteristic peaks at 400.78 and 399.28 eV, corresponding to the Co–N bond and C═N bond, respectively (Fig. 1d). Considering the method for the preparation of the COF-C_4N/THQ-Co sample, two NH_2 groups of some TPHA molecules may coordinate with Co, and then form the COF-C_4N structure at the THQ-Co edge with a phenazine bond (Fig. 1a). Compared to the C═N binding energy for COF-C_4N (400.0 eV), the binding energy for C═N in COF-C_4N/THQ-Co (399.28 eV) exhibits a negative shift by 0.72 eV, suggesting that THQ-Co interacts with COF-C_4N (Fig. S4). The Co 2p XPS spectra of THQ-Co and COF-C_4N/THQ-Co could be deconvoluted into four peaks (Fig. 1e). The peaks at 781.03 eV ($2p_{3/2}$) and 796.89 eV ($2p_{1/2}$) in THQ-Co, together with the satellite peaks at the binding energies of 785.48 and 801.27 eV can be attributed to the Co 2p of oxidized Co^{2+} species. The Co 2p spectrum of COF-C_4N/THQ-Co showed peaks at 780.74 and 796.58 eV, where their negative shifts by 0.29 and 0.31 eV, respectively, relative to THQ-Co indicate the existence of electron transport between COF-C_4N and THQ-Co on the surface of COF-C_4N/THQ-Co, which further proves that COF-C_4N grew at the edge of THQ-Co *via* Co–N. The C 1s spectrum of THQ-Co also reveals two characteristic peaks at 287.84 and 284.80 eV, which are attributed to C–O and C═C/C–C, respectively (Fig. 1f). Compared to THQ-Co, the C 1s spectrum of COF-C_4N/THQ-Co exhibits a new characteristic peak at 285.25 eV, which is assigned to the C═N bond and is negatively shifted by 0.15 eV relative to COF-C_4N (Fig. S4b). The shifts of the C═N peaks in both the N 1s and C 1s spectra verify that COF-C_4N grew at the edge of THQ-Co through phenazine bonding during the post-synthesis process, as shown in Fig. 1a. The peak at 532.08 eV in the O 1s spectrum corresponds to the O atom bonded to the metal (Co–O) from THQ-Co, indicating that the metal in THQ-Co is effectively coordinated with oxygen (Fig. 1g). In the O 1s spectrum of COF-C_4N/THQ-Co, the Co–O peak at 532.28 eV exhibits a positive shift of 0.20 eV relative to THQ-Co. This indicates that the NH_2 functional groups of COF-C_4N may coordinate with the Co sites to form Co–N bonds, enhancing bond polarity, and consequently increasing the binding energy. In short, the valence state of Co in both the THQ-Co and COF-C_4N/THQ-Co samples is +2. COF-C_4N grows at the edges of THQ-Co *via* both phenazine and Co–N bonds. Furthermore, the electron transfer capability between COF-C_4N and THQ-Co provides significant advantages for subsequent electrocatalytic reactions.

To further confirm the chemical composition and catalytic active sites in the prepared samples, we performed Raman measurements on THQ-Co, COF-C_4N, and COF-C_4N/THQ-Co, as shown in Fig. S5. In the Raman spectrum of THQ-Co, the peaks at 1292, 1337, 1447, 1510, and 1553 cm^{-1} are assigned to the stretching vibrations of the benzene rings in the organic binder and the Co–O coordination bonds formed between Co and the THQ ligands (black curve). In the spectrum of COF-C_4N, the different characteristic peaks appearing near ~1500 cm^{-1} correspond to the vibration of the C═N/C–N bonds in the phenazine structure, which is a signature structural signal of COF-C_4N (blue curve). After the formation of the composite, the Raman spectrum of COF-C_4N/THQ-Co exhibits peaks corresponding to the C–N bonds of COF-C_4N and Co–O/Co–N bonds of THQ-Co. The Co–N bonds originate from the coordination between the amino groups of TPHA and Co, indicating that COF-C_4N grew at the edges of THQ-Co *via* phenazine bonds and Co–N bonds (red curve). The Co–O/Co–N bonds can also serve as active sites for subsequent HER. Additionally, the Raman spectra of THQ-Co and COF-C_4N/THQ-Co exhibit a peak near approximately 450 cm^{-1}, which corresponds to the characteristic phase of $Co(OH)_2$. The $Co(OH)_2$ phase and the N sites adjacent to C in COF-C_4N synergistically act as active sites for the OER.

The Tauc plots from ultraviolet-visible diffuse reflectance spectroscopy (UV-vis) were used to study the band gaps of the

samples. The band gaps of THQ-Co, COF-C_4N, and COF-C_4N/THQ-Co are 2.83, 2.55, and 2.75 eV, respectively (Fig. S6). Fig. S7 and S8 show the flat-band potential (E_{fb}), which was obtained from the Mott–Schottky plot, and the conduction-band potentials were obtained using the following formula: $E_{CB\ NHE,pH=7} = E_{fb,Ag/AgCl,pH=7} + 0.197$. The conduction band (CB) values of THQ-Co, COF-C_4N, and COF-C_4N/THQ-Co are −0.78, −0.35, and −0.74 eV, respectively (Fig. S9, the Mott–Schottky results of THQ-M and COF-C_4N/THQ-M are also given in the SI). Based on the results derived from the UV-vis spectra and Mott–Schottky plots, the valence band energy level (VB) of THQ-M, COF-C_4N, and COF-C_4N/THQ-M could be obtained. According to Fig. S9, it can be found that the introduction of Fe in COF-C_4N/THQ-Fe, COF-C_4N/THQ-Co_1Fe_2, and COF-C_4N/THQ-Co_2Fe_1 caused their CB to be closer to 0.0 eV(NHE), which confirms that the HER activities of COF-C_4N/THQ-Fe, COF-C_4N/THQ-Co_1Fe_2, and COF-C_4N/THQ-Co_2Fe_1 would be lower than that of COF-C_4N/THQ-Co. The VB level for all the synthesized electrocatalysts is more positive than the OER electrical potential, and thus they are favorable for OER.

To confirm the sample morphology, we performed scanning electron microscopy (SEM) and transmission electron microscopy (TEM) measurements on THQ-Co, COF-C_4N, and COF-C_4N/THQ-Co. The SEM images showed that THQ-Co presented nanosheet-like structures with smaller nanosheets or agglomerated particles dispersed on their surface, and COF-C_4N also showed nanosheet-like structures with the agglomeration of the nanosheets (Fig. 2a and b, respectively), and EDS analysis of THQ-Co displayed that the C, O, and Co elements were uniformly distributed on its surface, and the content of Co was 10.68% (Fig. S10). It was also observed that the morphology of THQ-Co_2Fe_1 was similar to that of THQ-Co with a nanosheet-like structure, and its mass fraction ratio of Co to Fe wt% = 10.37 : 5.92, which was consistent with the mass ratio of the initial feed (Fig. S10). The SEM image of the COF-C_4N/THQ-Co samples also displayed a nanosheet-like structure with COF-C_4N dispersed on the surface and edges of THQ-Co and lamellar agglomeration, which is mainly due to the high plane conjugation of single-layer THQ-Co and COF-C_4N (Fig. 2c). The EDS elemental analysis in Fig. 2d indicated that C, N, O, and Co were uniformly dispersed in COF-C_4N/THQ-Co. According to inductively coupled plasma-optical emission spectrometry (ICP-OES), the content of Co(II) in THQ-Co and COF-C_4N/THQ-Co was determined to be 27.1 wt% and 15.6 wt%, respectively (Table S1). The TEM images further confirmed their morphologies. According to the TEM images in Fig. 2e and f, THQ-Co presents a flimsy nanosheet structure, and COF-C_4N/THQ-Co is clearly composed of two flimsy layered materials, in which COF-C_4N is regularly dispersed on their surface and at the edges of THQ-Co. This provides evidence from another perspective that COF-C_4N may grow at the edges of THQ-Co, leading to an increase in the number of exposed active sites in COF-C_4N/THQ-Co.

The porosity of THQ-Co, COF-C_4N, and COF-C_4N/THQ-Co was assessed by N_2 sorption isotherms at 77.3 K, as shown in Fig. S11. The Brunauer–Emmett–Teller (BET) surface areas of THQ-Co, COF-C_4N, and COF-C_4N/THQ-Co are 101.8, 71.8, and 50.4 $m^2\ g^{-1}$, respectively. The average pore sizes of THQ-Co, COF-C_4N, and COF-C_4N/THQ-Co determined using the BJH desorption data were 14.78 nm, 8.47 nm, and 14.19 nm, respectively. The pore volumes of the micropores and mesopores were determined using the HK and BJH methods, and their volume fractions were calculated, as shown in Table S2. All the samples exhibited mesopore-dominant structures. The results demonstrated that after the formation of the COF-C_4N composite, the BET specific surface area of the COF-C_4N/THQ-Co sample decreased. COF-C_4N likely partially filled the pore channels within and around THQ-Co, reducing

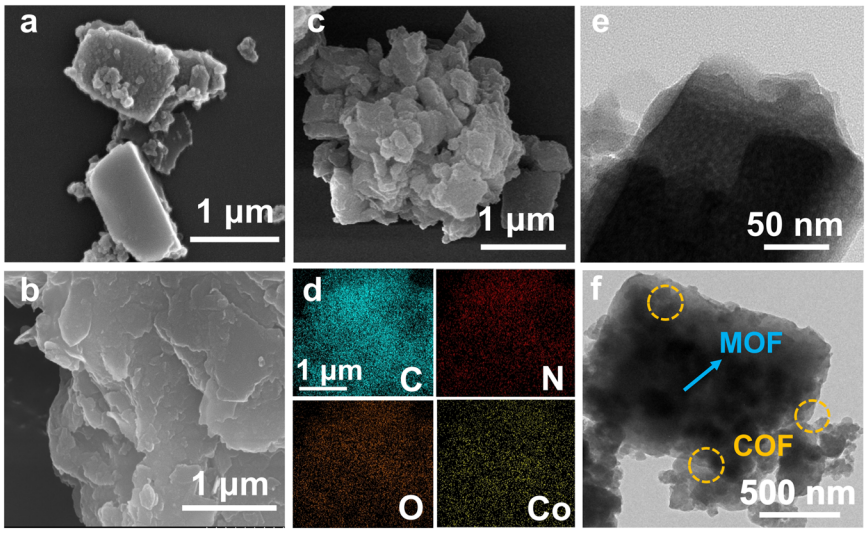

Fig. 2 SEM images of (a) THQ-Co, (b) COF-C_4N, and (c) COF-C_4N/THQ-Co; (d) EDS mappings of COF-C_4N/THQ-Co; and TEM images of (e) THQ-Co and (f) COF-C_4N/THQ-Co.

the effective pore volume available for nitrogen adsorption. The weak interactions between the two components at the interface led to locally denser structural packing, further diminishing the BET specific surface area of the composite samples. The average pore size of the composite samples was close to that of THQ-Co, indicating that the main pore structure of THQ-Co remained largely unchanged during the composite formation process.

2.2 Alkaline HER and OER

The electrocatalytic HER activities of the THQ-M and COF-C_4N/THQ-M catalysts were investigated using a typical three-electrode system in 1 M KOH alkaline solution with carbon cloth as the catalyst carrier. Linear sweep voltammetry (LSV) curves were recorded for the different catalysts. In 1 M KOH, the HER overpotential of THQ-Co is 89 mV at −10 mA cm^{-2}, whereas THQ-Ni and THQ-Cu did not display HER activity. THQ-Fe, THQ-Co_1Fe_2, and THQ-Co_2Fe_1 exhibited overpotentials of 237, 203, and 189 mV at −10 mA cm^{-2}, respectively. The test results suggest that Co serves as the best alkaline HER active site for THQ-M, and bimetal sites did not increase the alkaline HER activity of the catalysts (Fig. 3a). In contrast, for the composite catalyst, COF-C_4N/THQ-Co required only 58 mV to reach −10 mA cm^{-2}, and its alkaline HER activity was significantly enhanced. COF-C_4N/THQ-Fe, COF-C_4N/THQ-Co_1Fe_2, and COF-C_4N/THQ-Co_2Fe_1 with overpotentials of 188, 176, and 132 mV at −10 mA cm^{-2}, respectively, all exhibited improved HER activity compared to the single THQ-M MOF materials. Notably, even at a high current density of −100 mA cm^{-2}, COF-C_4N/THQ-Co still has a lower overpotential than the other catalysts, further validating its excellent alkaline HER activity (Fig. 3b). To further explore the HER reaction kinetics, the Tafel slopes of the catalysts were plotted by fitting the LSV curves to the linear regions of the Tafel plot ($\eta = b\log|j| + a$, where b is the Tafel slope, and j is the current density, with 100% iR compensation) (Fig. 3c and S12a). The Tafel slope of COF-C_4N/THQ-Co is 94.29 mV dec^{-1}, which is much smaller than that of THQ-Co (124.07 mV dec^{-1}), suggesting that the

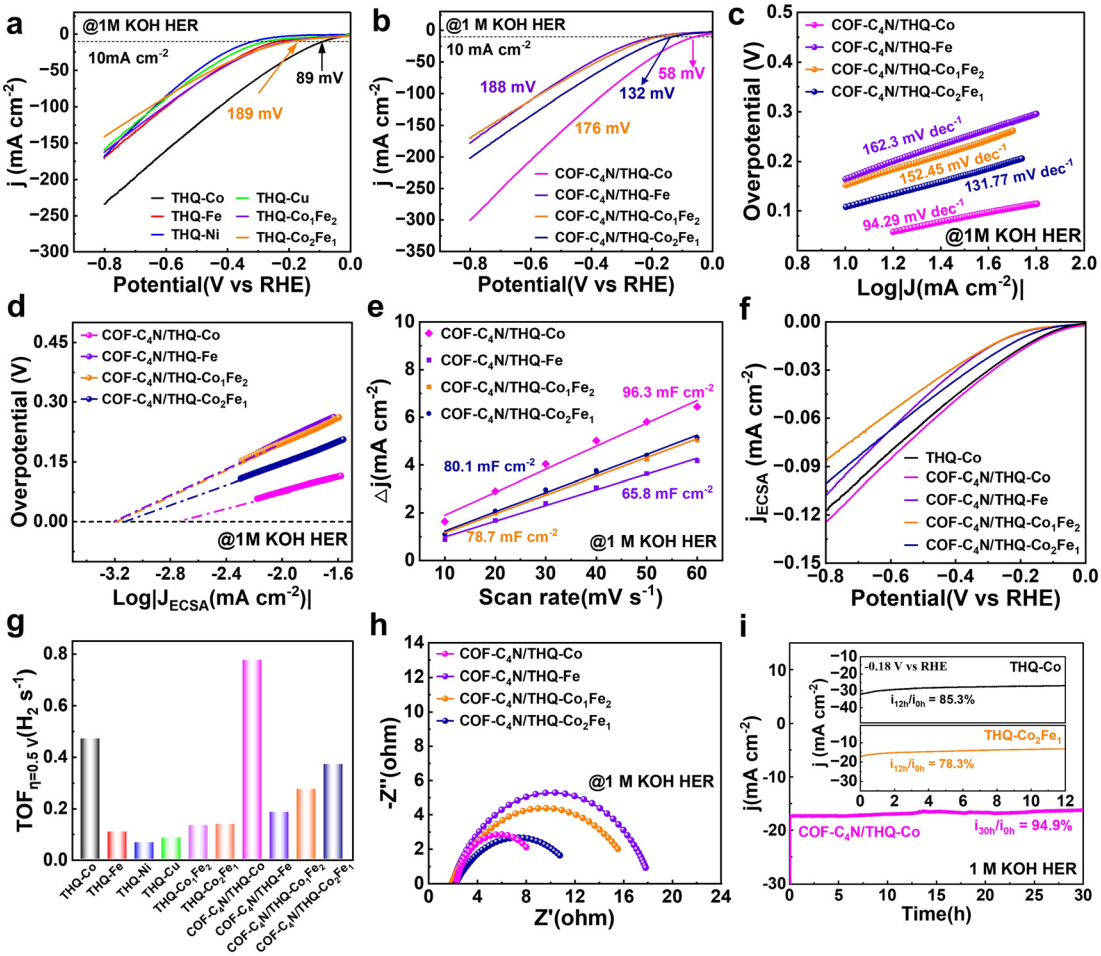

Fig. 3 (a) LSV curves of different metal THQ-M for the alkaline HER; (b) LSV curves of COF-C_4N/THQ-M; (c) Tafel slopes of COF-C_4N/THQ-M; (d) the exchange current density derived from the Tafel plot by an extrapolation method; (e) C_{dl} values of COF-C_4N/THQ-M; (f) the ECSA-normalized polarization curves of COF-C_4N/THQ-M; (g) comparison of TOF values for HER at η = 0.5 V; (h) EIS spectra of COF-C_4N/THQ-M; and (i) chronopotentiometric curves of COF-C_4N/THQ-Co at −0.11 V *vs.* RHE for 30 h (the insets are the chronopotentiometric curves of THQ-Co and THQ-Co_2Fe_1 at −0.18 V *vs.* RHE for 12 h).

composite catalyst has faster HER kinetics. Moreover, the Tafel slopes of 162.3, 152.45, and 131.77 mV dec^{-1} for COF-C_4N/THQ-Fe, COF-C_4N/THQ-Co_1Fe_2, and COF-C_4N/THQ-Co_2Fe_1 are lower than that of the corresponding THQ-M samples, respectively, which demonstrates that the formation of COF-C_4N/THQ-M is helpful to improve the kinetics of alkaline HER.

In general, the mechanism of HER in alkaline electrolyte is divided into two parts.[47] The first part is the Volmer reaction ($H_2O + e^- \rightarrow H^*_{ads} + OH^-$), where H_2O dissociates into H adsorbed on the catalyst surface. Subsequently, the second part has two pathways: (1) the Heyrovsky step ($H^*_{ads} + H_2O + e^- \rightarrow OH^- + H_2$), where H* combines with electrons and H_2O to form hydrogen molecules; and (2) the Tafel step ($H^*_{ads} + H^*_{ads} \rightarrow H_2$), where two H* atoms combine directly to form a hydrogen molecule. The Tafel slopes for the Volmer, Heyrovsky, and Tafel steps are usually considered to be 120, 40, and 30 mV dec^{-1}, respectively.[48] A smaller Tafel slope implies a faster kinetic process, suggesting that a lower overpotential is required for the catalyst to achieve the desired current. Thus, our synthesized COF-C_4N/THQ-Co composite catalysts follow the effective HER Volmer–Heyrovsky mechanism. The Heyrovsky reaction is the rate-determining step, and a larger electrode reaction area results in a faster electrolysis rate.[48] In addition, the exchange current density (j_0), which is proportional to the intrinsic HER activity of the electrocatalyst, can be derived from the Tafel plot by an extrapolation method.[49,50] In particular, after being normalized by the relative surface area, the j_0 obtained for COF-C_4N/THQ-Co was 1.77×10^{-3} mA cm^{-2}, which is much larger than that of COF-C_4N/THQ-Fe (0.62×10^{-3} mA cm^{-2}), COF-C_4N/THQ-Co_1Fe_2 (0.65×10^{-3} mA cm^{-2}), and COF-C_4N/THQ-Co_2Fe_1 (0.74×10^{-3} mA cm^{-2}) (Fig. 3d). Thus, the j_0 data also indicate that COF-C_4N/THQ-Co shows the highest HER activity.

To better explore the origin of the enhanced HER activity, the electrode area involved in the electrochemical process was revealed by the electrochemical surface area (ECSA). The ECSA was determined by measuring the double-layer capacitance (C_{dl}). The C_{dl} was obtained and calculated using the cyclic voltammetry (CV) curves recorded at different scan rates in 1 M KOH (Fig. 3e and S12b, S13, and S14). The calculated C_{dl} value of the COF-C_4N/THQ-Co was estimated to be 96.3 mF cm^{-2}, which is larger than that of THQ-Co (82.6 mF cm^{-2}) and the COF-C_4N/THQ-Fe (65.8 mF cm^{-2}), COF-C_4N/THQ-Co_1Fe_2 (78.7 mF cm^{-2}) and COF-C_4N/THQ-Co_2Fe_1 (80.1 mF cm^{-2}) composite catalysts, indicating that COF-C_4N/THQ-Co can expose more catalytically active sites, and a larger ECSA corresponds to enhanced HER catalytic activity (Fig. 3e). The ECSA-normalized LSV polarization curves (Fig. 3f) show that COF-C_4N/THQ-Co has higher current densities. Its overpotential is also lower than that of THQ-Co and the other mono/bimetallic composite catalysts. This also indicates that the HER activity was enhanced by constructing the composite catalyst, and the Co site mainly served as the active site for the alkaline HER.

To further elucidate the inherent HER activity of the catalysts, their turnover frequency (TOF) data were calculated. The number of active sites was determined by first performing CV in phosphate buffer (pH = 7) at a scan rate of 50 mV s^{-1}, as reported by Chen *et al.*[26] The TOF for HER was calculated using the following equation: TOF (s^{-1}) = ($j \times A$)/(2 $\times$ $n \times F$), where j, n, F, and A are the current density of the electrocatalyst, the number of active sites on the synthesized electrodes, the Faraday constant, and the cathode surface area, respectively. Fig. 3g shows the TOF data for THQ-M and COF-C_4N/THQ-M. COF-C_4N/THQ-Co requires lower overpotentials than the other catalysts. A TOF of 0.776 s^{-1} was obtained for the COF-C_4N/THQ-Co composite catalyst at an overpotential of η = 0.5 V, which is significantly higher than that of THQ-Co (0.47 s^{-1}) and the other composite catalysts (Fig. S15). Hence, the intrinsic HER activities of the composite catalysts follow the order of COF-C_4N/THQ-Co > THQ-Co > COF-C_4N/THQ-Co_2Fe_1 > COF-C_4N/THQ-Co_1Fe_2 > COF-C_4N/THQ-Fe > THQ-M (except for Co), confirming that the Co metal sites have higher HER activity, and that the synergistic effect between COF-C_4N and THQ-Co resulted in an increase in the HER activity of COF-C_4N/THQ-Co. Moreover, electrochemical impedance spectroscopy (EIS) analysis was performed to study the HER kinetics of the catalysts. The Nyquist plots (Fig. 3h and S11c) indicated that the charge transfer resistance (R_{ct}) of all the composite catalysts is lower than that of THQ-M. The R_{ct} of COF-C_4N/THQ-Co is 7.12 Ω cm^{-2}, which is lower than that of THQ-Co (8.90 Ω cm^{-2}), COF-C_4N/THQ-Fe (16.4 Ω cm^{-2}), COF-C_4N/THQ-Co_1Fe_2 (15.3 Ω cm^{-2}), and COF-C_4N/THQ-Co_2Fe_1 (10.2 Ω cm^{-2}). This suggests that the charge transfer kinetics of COF-C_4N/THQ-Co is faster than single THQ-Co during the HER process.

In addition to catalytic activity, stability is crucial for the practical application of catalysts. The long-term stability of the catalysts was further evaluated by continuous CV scanning for 500 cycles, and chronoamperometric tests were carried out under a constant overpotential in 1 M KOH. Fig. S16 presents the LSV polarization curves of the COF-C_4N/THQ-Co composite before and after 500 CV cycles. The LSV polarization curves show little change, and the current density decay of COF-C_4N/THQ-Co was negligible after the 500 CV cycles, indicating its robust stability for alkaline HER. Furthermore, COF-C_4N/THQ-Co displayed obviously enhanced stability in the chronoamperometry test in comparison with THQ-Co (85.3% for 12 h), THQ-Co_2Fe_1 (78.3% for 12 h), and COF-C_4N/THQ-Co (95.7% for 12 h, Fig. S17), maintaining a current density of 94.9% under a constant potential test for 30 h. Therefore, the composite of COF-C_4N and THQ-Co not only exhibits enhanced HER activity but also improved catalytic stability in alkaline solution (Fig. 3i).

The electrocatalytic OER performance of the samples was also tested in alkaline medium. The LSV curves of THQ-M for OER in 1 M KOH are presented in Fig. 4a. It can be observed that the overpotential of THQ-Co is 357 mV at 10 mA cm^{-2},

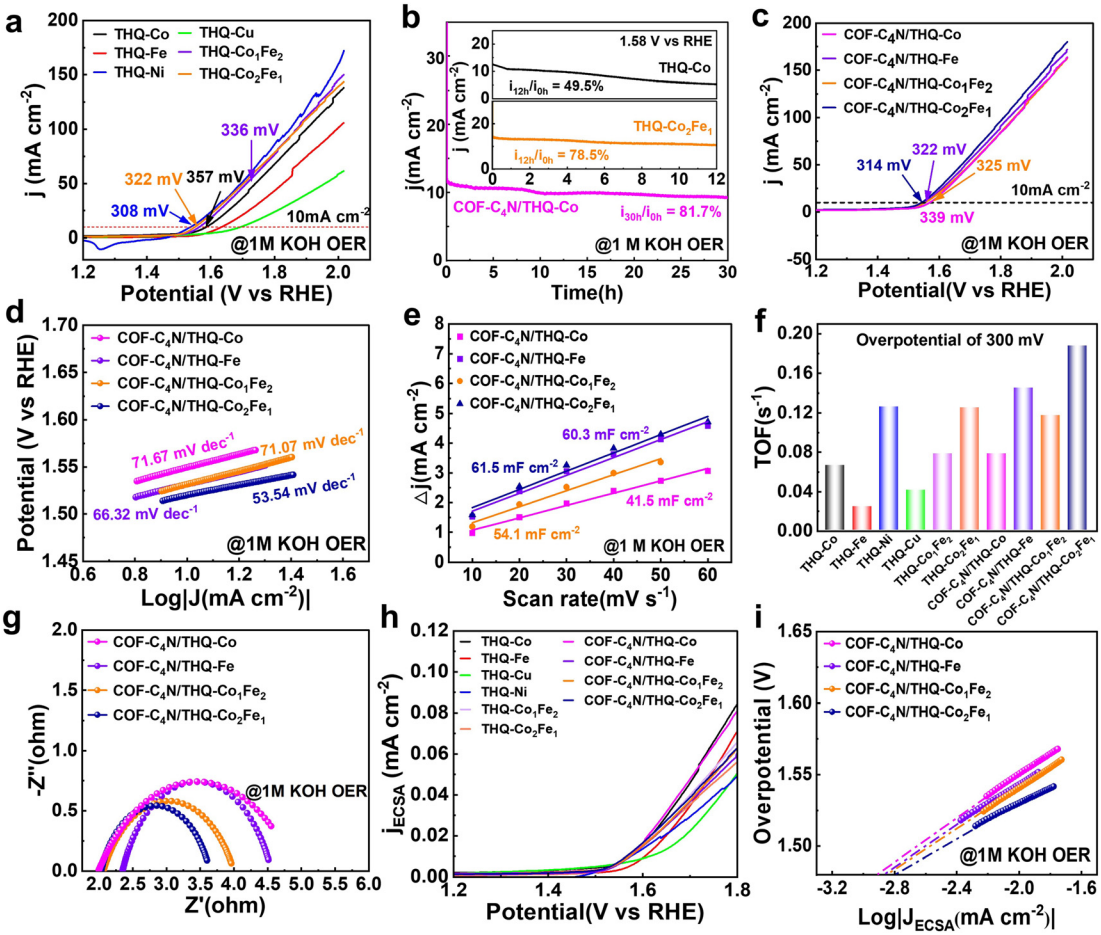

Fig. 4 (a) LSV curves of different metal THQ-M for the alkaline OER; (b) chronopotentiometric curves of THQ-Co and THQ-Co_2Fe_1 at 1.58 V *vs.* RHE for 12 h and (inset) chronopotentiometric curves of COF-C_4N/THQ-Co for 30 h; (c) LSV curves of COF-C_4N/THQ-M; (d) Tafel slopes of COF-C_4N/THQ-M; (e) C_{dl} values of COF-C_4N/THQ-M for the OER in alkaline medium; (f) comparison of TOF values for OER at η = 300 mV; (g) EIS spectra of COF-C_4N/THQ-M; (h) the ECSA-normalized polarization curves; and (i) the exchange current density derived from the Tafel plot by an extrapolation method.

and the overpotentials of THQ-Fe and THQ-Cu are larger (405 mV and 465 mV at 10 mA cm^{-2}). THQ-Ni displays an oxidation peak, although negative sweeping caused its overpotential to reach 308 mV at 10 mA cm^{-2}. The stability test of THQ-Co shows that the current density of the sample decreased significantly under a continuous constant potential test for 12 h, only 49.5% of its current density was maintained, and its catalytic activity decreased dramatically, which indicates its poor electrocatalytic OER stability (Fig. 4b). The XRD spectra of THQ-Co before and after electrocatalysis varied considerably, as shown in Fig. S18, and the diffraction peaks of THQ-Co disappeared after electrocatalysis. This result indicates that its structural instability led to poor electrocatalytic OER stability. Its structure underwent obvious changes, probably due to Co^{2+} dislodging from its structure during prolonged testing, which led to the continuous disintegration of its structure and gradual degradation of OER performance. In comparison, the bimetallic THQ-Co_2Fe_1 exhibited enhanced OER activity and moderate stability (322 mV at 10 mA cm^{-2}, 78.5%) (Fig. 4b). The smaller R_{ct} of the bimetallic catalysts also indicates their enhanced charge transfer kinetics, accelerated electron transfer process, and enhanced catalytic OER performance (Fig. S19).

The COF-C_4N/THQ-M composites were constructed and synthesized to further enhance the OER activity and stability. As observed in the LSV curves in Fig. 4c, the OER overpotentials of COF-C_4N/THQ-Co, COF-C_4N/THQ-Fe, COF-C_4N/THQ-Co_1Fe_2, and COF-C_4N/THQ-Co_2Fe_1 at 10 mA cm^{-2} are 339, 322, 325, and 314 mV, respectively. The OER overpotentials of all the COF-C_4N/THQ-M composites are lower than that of the corresponding single THQ-M. Also, the Tafel slopes of the composites are all smaller than that of the THQ-M samples (Fig. 4d and S19a). The Tafel slope of COF-C_4N/THQ-Co_2Fe_1 is 53.54 mV dec^{-1}, which indicates that it has a relatively faster charge transfer rate in the OER process (Fig. 4d). The calculated C_{dl} of all COF-C_4N/THQ-M is found to be higher than the corresponding single THQ-M, indicating that the COF-C_4N/THQ-M composites have larger electrochemically active areas and can expose more active

sites compared to THQ-M (Fig. 4e and S19–S21). Among them, COF-C_4N/THQ-Co_2Fe_1 has the largest C_{dl} value and displays the optimal OER activity. The TOF of COF-C_4N/THQ-Co_2Fe_1 is also higher than all the other composite catalysts and THQ-M, as given in Fig. 4f. For example, at an overpotential of 300 mV, COF-C_4N/THQ-Co_2Fe_1 achieved a TOF of 0.19 s^{-1}, which is slightly higher than that of COF-C_4N/THQ-Co (0.078 s^{-1}), COF-C_4N/THQ-Fe (0.145 s^{-1}), COF-C_4N/THQ-Co_1Fe_2 (0.117 s^{-1}), THQ-Co (0.066 s^{-1}), and THQ-Fe (0.024 s^{-1}) (Fig. 4f and S22). The enhanced activity of COF-C_4N/THQ-Co_2Fe_1 may be attributed to the synergistic interaction between Co and Fe. In addition, the R_{ct} values of COF-C_4N/THQ-Co, COF-C_4N/THQ-Fe, COF-C_4N/THQ-Co_1Fe_2, and COF-C_4N/THQ-Co_2Fe_1 are all smaller than that of the corresponding THQ-M according to their Nyquist curves (Fig. 4g and S19c). Among the composite catalysts, COF-C_4N/THQ-Co_2Fe_1 displays the smallest R_{ct} and the best conductivity owing to its superior charge transfer. Moreover, the ECSA-normalized LSV polarization curves in Fig. 4h indicate that COF-C_4N/THQ-Co_2Fe_1 has the highest current density. Fig. 4i shows the exchange current density obtained from the Tafel plot by an extrapolation method, indicating that COF-C_4N/THQ-Co_2Fe_1 displays the highest value. All these data demonstrate that COF-C_4N/THQ-Co_2Fe_1 exhibits the optimal OER activity.

LSV tests were performed before and after 500 CV cycles for COF-C_4N/THQ-Co, COF-C_4N/THQ-Fe, COF-C_4N/THQ-Co_1Fe_2, and COF-C_4N/THQ-Co_2Fe_1 (Fig. S23). It was observed that the current density decay of COF-C_4N/THQ-Co was negligible after 500 CV cycles. A chronoamperometric test was subsequently performed at a constant potential to evaluate the OER stability of COF-C_4N/THQ-Co in 1 M KOH. The results show that 81.7% of the current density was maintained after 30 h (Fig. 4b). Thus, the results confirmed that forming composite catalysts is beneficial for further enhancing the alkaline OER stability.

To further investigate the catalytic stability of the COF-C_4N/THQ-Co sample, we performed ICP testing on its Co(II) content after 500 cycles CV. Its Co elemental content after the HER and OER cycles was 13.54 wt% and 11.69 wt%, respectively (Table S3). The results revealed slight leaching of Co during the electrocatalytic cycle, which is presumed to originate from the dissociation and dissolution of the active sites during the reaction process. The strong oxidative environment of the OER exacerbates Co leaching, consistent with the results from the 30 h chronopotentiometric curve of COF-C_4N/THQ-Co (Fig. 4b). This indicates that Co leaching may be one of reasons leading to the slight decrease in the OER stability. Combined with the LSV curves of COF-C_4N/THQ-Co after 500 cycles of OER and HER (Fig. S16 and S23) and the chronopotentiometric curves after 30 h, the catalytic activity did not decrease much after cycling on the whole. Therefore, although a small amount of Co leaching occurs in the COF-C_4N/THQ-Co sample, its activity and stability were not significantly affected. COF-C_4N/THQ-Co after a 30 h chronoamperometric test for HER and OER was characterized by XRD, IR, SEM, and TEM (Fig. S24–S26). The results demonstrate that the morphology and crystal structure of COF-C_4N/THQ-Co after the stability test slightly varied in alkaline medium compared with the pristine COF-C_4N/THQ-Co. Subsequently, XPS analysis was performed on the COF-C_4N/THQ-Co sample before and after HER/OER catalysis to determine their composition. The Co 2p spectrum after HER revealed a slight shift in the Co $2p_{3/2}$ peak toward a lower binding energy without broadening, indicating the good structural stability of the catalyst during HER and no significant dissolution or loss of Co (Fig. S27a). As shown in Fig. S27b, following the OER stability test, two primary peaks appear at 780.03 and 782.19 eV in its Co $2p_{3/2}$ spectrum. The peak at 782.19 eV corresponds to Co^{3+} $2p_{3/2}$, while the satellite peak at 788.27 eV exhibits a reduced intensity and a shift, confirming the presence of a small amount of residual Co^{2+}. This indicates that Co undergoes oxidation during the OER process, with the low-valent Co^{2+} being oxidized to higher oxidation states. Additionally, the reduced intensity of the Co 2p peak after the reaction suggests that some Co dissolved and was lost under the high-potential and strongly alkaline OER conditions, leading to a decrease in Co content on the catalyst surface. This finding is consistent with the ICP test results.

Based on the discussion above, all four highly conjugated composites COF-C_4N/THQ-Co, COF-C_4N/THQ-Fe, COF-C_4N/THQ-Co_1Fe_2, and COF-C_4N/THQ-Co_2Fe_1 display efficient electrocatalytic bifunctional HER and OER activity under alkaline conditions. According to the comparison of their alkaline HER and OER activity with other works, as shown in Fig. 5a and b, the alkaline HER activity of COF-C_4N/THQ-Co

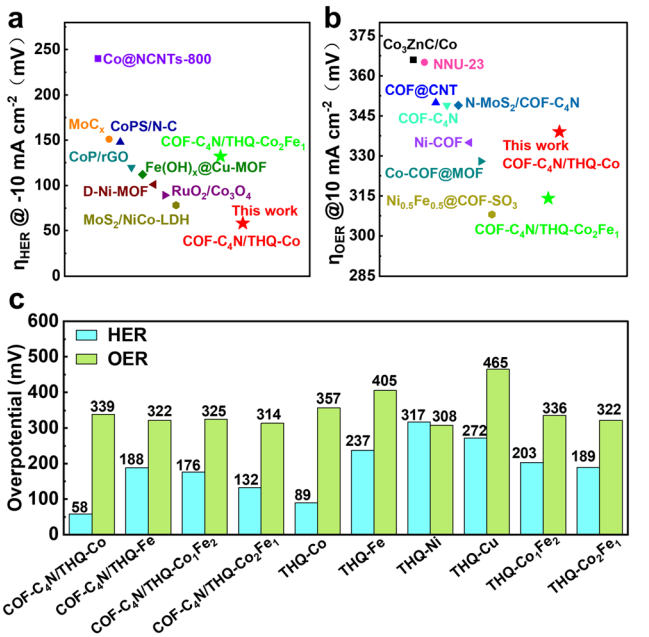

Fig. 5 Comparison of the (a) OER and (b) HER activities of our catalysts with those of recently reported electrocatalysts on various substrates in an alkaline medium. (c) Comparison of the HER and OER activities of the different catalysts we prepared in alkaline medium.

reaches the current optimal level (Table S4), and the OER activities of COF-C_4N/THQ-Co and COF-C_4N/THQ-Co_2Fe_1 are comparable to that of other non-noble metal OER catalysts (Table S5). Fig. 5c displays a comparison of the OER and HER overpotentials at 10 mA cm^{-2} and −10 mA cm^{-2} for the different catalysts in this work, where COF-C_4N/THQ-Co and COF-C_4N/THQ-Co_2Fe_1 are proposed to be the optimal alkaline HER and OER electrocatalysts, respectively, in this work.

To further reveal the influence of the synthesis method and composition mode on the electrocatalytic HER/OER activity and stability of these catalysts, we prepared COF-C_4N + THQ-M catalysts by simply mixing the COF-C_4N samples and THQ-M samples at a mass ratio of 1 : 1, and then subjecting them to ultrasonically dispersion. The OER and HER activity of COF-C_4N + THQ-M in 1 M KOH was also tested. Fig. S28 and S29 show that the HER overpotentials of the four COF-C_4N + THQ-M samples are 83, 246, 187, and 173 mV at 10 mA cm^{-2} and their Tafel slopes are 120, 283, 178, and 159 mV dec^{-1}, respectively. The HER activities all decreased relative to COF-C_4N/THQ-M. The HER stability test for COF-C_4N + THQ-Co was performed as shown in Fig. S28d, where the current density was only maintained at 71.1% under a 12 h constant potential test. The OER activity tests in Fig. S30 and S31 indicate that the OER overpotentials of COF-C_4N + THQ-Co, COF-C_4N + THQ-Fe, COF-C_4N + THQ-Co_1Fe_2, and COF-C_4N + THQ-Co_2Fe_1 at 10 mA cm^{-2} are 346, 422, 337, and 321 mV, respectively. The current density for COF-C_4N + THQ-Co_2Fe_1 remained 79.1% under a 12 h constant potential test, as shown in Fig. S30d. Overall, the activity and stability of COF-C_4N + THQ-M are not as good as that of COF-C_4N/THQ-M, regardless of HER or OER. Fig. S32 compares the HER/OER LSV polarization curves of COF-C_4N/THQ-Co_2Fe_1 and COF-C_4N + THQ-Co_2Fe_1 prepared by two different methods. The HER activity of COF-C_4N + THQ-Co_2Fe_1 could not reach that of COF-C_4N/THQ-Co_2Fe_1 prepared *via* the post-synthesis method. The difference in OER activity between COF-C_4N/THQ-Co_2Fe_1 and COF-C_4N + THQ-Co_2Fe_1 is relatively small. The comparison of the activity results combined with the characterization analysis of COF-C_4N/THQ-M indicates that the post-synthesis method perhaps allows a portion of COF-C_4N to grow at the edges of THQ-M *via* Co–N or phenazine bonding, thereby preventing the disintegration of the THQ-M structures, exposing more metal sites of THQ-M for HER/OER, and effectively promoting charge transfer and separation to realize enhanced activity and stability for HER/OER.

2.3 Mechanism

The HER process in alkaline media requires the dissociation of H_2O at the catalyst surface to obtain protons. Thus, the HER process in alkaline media involves two steps (Fig. 6a), the Volmer step ($H_2O + e^- \rightarrow *H + OH^-$) and the Heyrovsky step ($H_2O + *H + e^- \rightarrow H_2 + OH^-$). In the alkaline HER, the first step requires the appropriate adsorption of H_2O molecules on the catalyst surface. The H_2O adsorption step on COF-C_4N requires

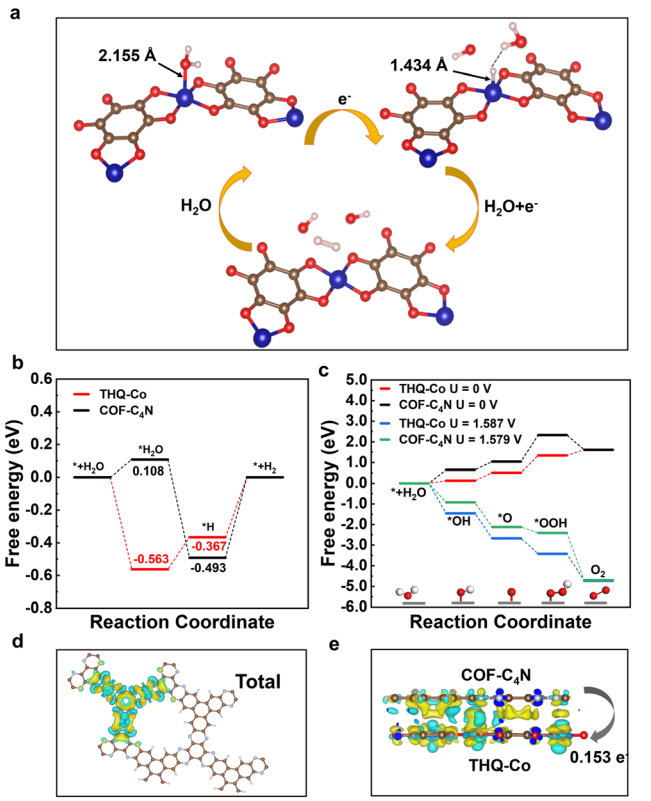

Fig. 6 Mechanisms of THQ-Co and COF-C_4N for the OER and HER in alkaline media. (a) Schematic of the proposed HER pathway on the surface of the THQ-Co catalyst in alkaline media; (b) the free energy profiles for the HER process for THQ-Co and COF-C_4N catalysts in alkaline media; (c) the free energy profiles for the OER process at the Co sites for THQ-Co and C4 sites for COF-C_4N at applied potential bias and U = 0 V (pH = 14); (d) charge density difference ($\Delta\rho$) for a model structure of COF-C_4N growing at the edge of THQ-Co (isovalue, 0.0025 e $Å^{-3}$), $\Delta\rho = \rho_{AB} - \rho_A - \rho_B$, where set AB is the total model structure, set A is the metal atoms, and set B is the residual part after subtracting the metal atoms; and (e) charge density difference for a model structure of COF-C_4N interacting with THQ-Co with π–π interaction, $\Delta\rho = \rho$(total) − ρ(THQ-Co) − ρ(COF-C_4N). The yellow and blue isosurfaces indicate charge accumulation and charge depletion in space, respectively.

an overcoming energy barrier of 0.108 eV, but H_2O adsorption on the Co site of THQ-Co is very easy and is an thermodynamically favorable process (ΔG_{H_2O} = −0.563 eV, as shown in Fig. 6b). Although H_2O dissociation to generate *H requires overcoming an energy barrier of about 0.2 eV for THQ-Co, H_2 desorption from the Co site of THQ-Co is easier than from the N site of COF-C_4N according to that comparison of $|\Delta G_{*H}|$ at the Co site and N site in Fig. S33. The alkaline HER overpotential of COF-C_4N measured experimentally is 253 mV at 10 mA cm^{-2} (Fig. S34), further verifying that COF-C_4N exhibits poor activity for HER. Therefore, the above-mentioned results demonstrate that Co sites are the main HER active centers for both THQ-Co and the COF-C_4N/THQ-Co composite catalyst. The further enhancement in the HER activity of the COF-C_4N/THQ-Co composite catalysts should be attributed to the increased charge transfer between COF-C_4N and THQ-Co.

To gain insight into the OER activity, we calculated the free energy profiles of the OER pathways for THQ-Co and COF-C_4N at U = 0 V and experimentally applied bias, respectively, as shown in Fig. 6c, in which the OER active sites are the Co sites for THQ-Co and C4 sites for COF-C_4N (ref. 43) (the intermediate configurations in the OER pathway for THQ-Co are shown in Fig. S35). The energy barriers of the rate-determining step *O → *OOH for both THQ-Co and COF-C_4N are 0.83 eV and 1.28 eV, respectively. When the applied bias of THQ-Co and COF-C_4N is considered, they both show a spontaneous downhill tendency at the actual applied bias of 1.587 V and 1.579 V, respectively, which proves that they display similar OER activity at a small applied bias. The electrocatalytic OER stability of the separate THQ-Co is very poor, and therefore the composite of THQ-Co and COF-C_4N not only exhibited improved stability but also further improved OER activity because COF-C_4N could increase the number of OER active sites and accelerate the charge transfer.

As shown in Fig. 6d and e, we calculated the charge density differences for COF-C_4N/THQ-Co. It is clear that electrons are more accumulated on the Co sites in the model structure of COF-C_4N growing at the edge of THQ-Co, as shown in Fig. 6d. As shown in Fig. 6e, the electrons are locally accumulated at the interface region of COF-C_4N and THQ-Co for the model structure of COF-C_4N on the surface of THQ-Co by π–π interaction, which significantly regulated the electronic structure of the COF-C_4N/THQ-Co composites, and the electrons transferred from the COF-C_4N layer to the surface of THQ-Co with 0.153 e^-. The charge density differences verified that the charge transfer abilities are enhanced and the electrons will migrate to the surface of THQ-Co to produce H_2 at the Co sites.

3 Conclusions

In conclusion, two highly conjugated 2D materials, COF-C_4N and THQ-M, were chosen for the first time to prepare COF/MOF composite electrocatalysts, COF-C_4N/THQ-M, *via* a post-synthesis strategy. The characterization and tests showed that a part of COF-C_4N may grow at the edge of THQ-M, besides its uniform dispersion on the surface of THQ-M. Their HER and OER activity and stability in alkaline media were systematically studied and compared. The results indicate that the composite of THQ-M and COF-C_4N not only exhibited improved stability, but also further enhanced HER/OER activity compared to the corresponding single THQ-M and COF-C_4N. Based on the regulation of their metal sites, COF-C_4N/THQ-Co and COF-C_4N/THQ-Co_2Fe_1 are proposed to be the optimal alkaline HER and OER electrocatalysts, respectively, in this work. DFT calculations revealed that both THQ-Co and COF-C_4N can act as OER catalysts, and COF-C_4N in the composite catalysts COF-C_4N/THQ-Co mainly solved the instability of THQ-Co in alkaline media. THQ-Co can act as an HER catalyst alone, but its composite with COF-C_4N realizes more effective HER activity and stability in alkaline media. The charge density difference was also calculated to verify the charge transfer in COF-C_4N/THQ-M. This study provides a new proposal for the design of highly efficient bifunctional COF/MOF composite electrocatalysts.

4 Experimental section

4.1 Chemicals and materials

All reagents were directly obtained from commercial sources and used as received without further purification. Cobalt chloride hexahydrate ($CoCl_2{\cdot}6H_2O$), ferrous sulfate heptahydrate ($FeSO_4{\cdot}7H_2O$), nickel acetate tetrahydrate ($Ni(OAc)_2{\cdot}4H_2O$), copper(II) acetate monohydrate ($Cu(OAc)_2{\cdot}H_2O$), Nafion solution (5.0 wt%), sodium hydroxide, potassium hydroxide, and acetic acid were purchased from Shanghai Rinn Technology Development Co., Ltd. Iron(III) chloride hexahydrate was purchased from Tianjing HengXing Chemical Reagent Co., Ltd. Tetrahydroxyquinone was purchased from Shandong Xiya Reagent Co., Ltd. 2,3,6,7,10,11-Triphenylenehexamine hexahydrochloride and hexaketocyclohexane octahydrate were purchased from Jilin Chinese Academy of Sciences-Yanshen Technology Co., Ltd. 1,3,5-Trimethylbenzene (3 mL) was purchased from Nanning Chemical Group Co., Ltd. 1,4-Dioxane was purchased from Shanghai Aladdin Biochemical Technology Co., Ltd. Carbon cloth was purchased from Suzhou Sinero Technology Co., Ltd. A graphite rod and Ag/AgCl (3.5 M KCl) electrode were purchased from AIDA Science-Technology Development Co., Ltd. All aqueous solutions were prepared using ultrapure water.

4.2 Synthesis of catalysts

Synthesis of THQ-M: the THQ-M samples were synthesized according to a reported procedure with minor modifications.[44,45] In a typical synthesis of THQ-Co, 0.135 mmol of $CoCl_2{\cdot}6H_2O$ was completely dissolved in 16 mL of deionized water, and then 40 μL of ethylenediamine was injected into the above-mentioned solution using a pipette gun. Then, 0.29 mmol of tetrahydroxy-1,4-quinone (THQ) was completely dissolved in 16 mL of deionized water, and then transferred to the above-mentioned water/ethylenediamine solution under ultrasonic vibration. The mixed solution was poured into a sealed glass vial and heated at 85 °C for 12 h. After cooling naturally to room temperature, the precipitate was collected and washed with water and ethanol for 30 min in an ultrasonic ice bath, and then left to settle. After, it was filtered and washed three times with water and acetone, respectively. Finally, it was vacuum dried at 60 °C for 24 h to obtain THQ-Co. THQ-Fe, THQ-Ni, THQ-Cu, THQ-Co_1Fe_2, and THQ-Co_2Fe_1 were synthesized in a similar way using different $Ni(OAc)_2{\cdot}4H_2O$, $Cu(OAc)_2{\cdot}H_2O$, and $FeSO_4{\cdot}7H_2O$, with the total amount of metal ions fixed at 0.27 mmol.

Synthesis of COF-C_4N/THQ-Co: 2,3,6,7,10,11-triphenylenehexamine hexahydrochloride (TPHA) and hexaketocyclohexane octahydrate (HKH) were weighed in a mass ratio of 25.5 mg : 25.0 mg. The above-mentioned

samples were dissolved in a mixture of 1.5 mL of 1,4-dioxane and 1.5 mL of 1,3,5-trimethylbenzene in a 10 mL tube, and 50 mg of the THQ-Co sample was added. It was dispersed by sonication at 25 °C for 30 min, and then 4 M acetic acid (0.5 mL) added to the test tube and shaken well. Next, three freeze–pump–thaw cycles were performed. After degassing and confinement, the reaction was carried out in a blower oven at 150 °C for 3 days, and then cooled naturally to room temperature. The precipitate was washed with tetrahydrofuran and acetone (30 mL × 3), and thoroughly cleaned by Soxhlet extraction with tetrahydrofuran for 10 h. Finally, it was vacuum-dried at 120 °C under reduced pressure (−0.09 MPa) for 12 h to obtain the final product COF-C_4N/THQ-Co in black solid form. COF-C_4N/THQ-Fe, COF-C_4N/THQ-Co_1Fe_2, and COF-C_4N/THQ-Co_2Fe_1 were synthesized using the same procedure.

Synthesis of COF-C_4N + THQ-M: the prepared COF-C_4N samples were mixed with the THQ-M samples at a mass ratio of 1 : 1 and ultrasonically dispersed by adding ethanol for 30 min, followed by stirring for 24 h. At the end of the reaction, filtration–washing–drying were carried out to obtain the simple COF-C_4N + THQ-M composite catalyst.

4.3 Materials characterization

The structure, composition, and texture properties of the materials were studied *via* powder X-ray (PXRD) diffraction (TD-3700 X-ray diffractometer), Fourier transform infrared (FT-IR) spectroscopy (Equinox 55), scanning electron microscopy (SEM) (EVO18), and transmission electron microscopy (TEM) (JEM-2100 electron microscope). X-ray photoelectron spectroscopy (XPS) measurements were performed using a Thermo Scientific K-Alpha and the C 1s peak at 284.6 eV as the internal standard. Inductively coupled plasma-optical emission spectrometry (ICP-OES) was carried out using an Agilent ICP-OES 725 ES. The nitrogen adsorption/desorption isotherms were evaluated at 77.3 K on Autosorb-1Q3, and the methods of Brunauer–Emmett–Teller (BET) and Barrett–Joyner–Halenda (BJH) were applied to get specific surface area and pore size distribution.

4.4 Electrochemical measurements

All electrochemical measurements were conducted at room temperature using a standard three-electrode CHI660E (Shanghai Chenhua) electrochemical workstation. Ag/AgCl and a graphite rod were used as the reference and counter electrodes, respectively, and conductive carbon cloth fibers with deposited catalysts were used as the working electrodes for evaluating the HER and OER activity of the various catalysts. Electrochemical experiments were carried out on HER and OER in 1.0 M KOH solution. Before the electrochemical measurements, the 1.0 M KOH alkaline electrolyte was purged with N_2 gas for 30 min. All potentials at the reversible hydrogen electrode (RHE) were reported and converted using the following equation (eqn (1)):

$$E_{vs.\ \mathrm{RHE}} = E_{vs.\ \mathrm{Ag/AgCl}} + 0.2046\ \mathrm{V} + 0.059\ \mathrm{V} \times \mathrm{pH} \quad (1)$$

In the cyclic voltammetry (CV) tests, the potential range was circularly scanned at the OER potential range of 0–1.0 V (*vs.* Ag/AgCl) and the HER potential range of −1–−1.82 V (*vs.* Ag/AgCl) at a scan rate of 50 mV s^{-1}. After 20 CV cycles, the linear sweep voltammetry (LSV) test was conducted at a scan rate of 5 mV s^{-1} over the same potential range. The HER and OER overpotentials (η) were calculated according to eqn (2) and (3), as follows:

$$\eta_{\mathrm{OER}} = E_{vs.\ \mathrm{RHE}} - 1.23\ \mathrm{V} \quad (2)$$

$$\eta_{\mathrm{HER}} = E_{vs.\ \mathrm{RHE}} \quad (3)$$

The Tafel slope was estimated by linear fitting of the polarization curves according to Tafel eqn (4).

$$\eta = a + b\log(j) \quad (4)$$

where j is the current density and b is the Tafel slope.

To evaluate the double-layer capacitance (C_{dl}), CV was performed by applying different scan rates over a specific voltage range, and the difference in current density at the midpoint of the voltage range was selected for processing, which is linearly related to the corresponding scan rate, where the slope is the C_{dl} value. The active surface area of the catalyst can be inferred by comparing the C_{dl} size of several samples.

Electrochemical impedance spectroscopy (EIS), with potential conditions corresponding to a current density of 10 mA cm^{-2}, was performed in the frequency range of 0.01 Hz to 105 Hz, and data such as the internal resistance and charge transfer resistance of the different samples were compared by analyzing their test curves. Chronoamperometric measurement at constant potentials of 1.58 V (*vs.* RHE) and −0.18 V (*vs.* RHE) was performed to test the HER and OER stability of the samples.

Mott–Schottky tests were performed in a three-electrode cell using the Ag/AgCl electrode as the reference electrode at 500, 700, and 900 Hz to record the curves.

TOF calculation. The turnover frequency (TOF) for each active site was determined by employing previously reported methods. Firstly, we recorded cyclic voltammograms in phosphate buffer (pH = 7) at a scan rate of 50 mV s^{-1} to examine the number of active sites (n). Then, the number of voltammetric charges (Q) can be obtained after the blank value has been deducted. Therefore, n (mol) and TOF (s^{-1}) can be determined toward HER using eqn (5) and (6), as follows:

$$n = \frac{Q}{2F} \quad (5)$$

$$\mathrm{TOF} = \frac{j \times S_{\mathrm{geo}}}{2 \times n \times F} \quad (6)$$

Toward OER, the n (mol) and TOF (s^{-1}) can be determined using the following equations:

$$n = \frac{Q}{4F} \tag{7}$$

$$\mathrm{TOF} = \frac{j \times S_{\mathrm{geo}}}{4 \times n \times F} \tag{8}$$

where j is the measured current density, S_{geo} (1.0 cm^2) is the surface area of CFC, and F is the Faraday constant (96 485.3 C mol^{-1}).

4.5 Calculation methods

Density functional theory (DFT) was used to calculate all geometrical and electron structures. The interaction between the core and valence electrons is described using the frozen-core projector augmented wave (PAW) approach.[51–53] The generalized gradient approximation of the Perdew–Burke–Ernzerhof (PBE) functional was used.[53] The energy cutoff was set to be 500 eV. A Γ-centered mesh of 3 × 3 × 1 k-points was used to sample the two-dimensional Brillouin zone. The van der Waals (vdW) correction proposed by Grimme was adopted to describe long-range vdW interactions. A vacuum space greater than 15 Å perpendicular to the sheet was applied so that the interaction between neighboring slabs was negligible. All geometry structures were fully relaxed until the convergence criteria of energy and force are less than 1×10^{-5} eV and 0.01 eV $Å^{-1}$, respectively.

The binding energies of H, OH, and H_2O were calculated using eqn (9)–(11), respectively.

$$\Delta E_{\mathrm{H}}^{\mathrm{b}} = E_{\mathrm{H}*} - E_{*} - 0.5E_{\mathrm{H_2}} \tag{9}$$

$$\Delta E_{\mathrm{H_2O}}^{\mathrm{b}} = E_{\mathrm{H_2O}*} - E_{*} - E_{\mathrm{H_2O}} \tag{10}$$

$$\Delta E_{\mathrm{OH}}^{\mathrm{b}} = E_{\mathrm{OH}*} - E_{*} - E_{\mathrm{H_2O}} + 0.5E_{\mathrm{H_2}} \tag{11}$$

where $E_{\mathrm{H}*}$, $E_{\mathrm{OH}*}$, and $E_{\mathrm{H_2O}*}$ are the energies of H, OH, and H_2O absorbed on the catalyst surface, respectively. $E_{\mathrm{H_2O}*}$ is the energy of the H_2O molecule in the gaseous phase.

Calculation of free energy difference: the free energy difference for OER was calculated according to eqn (12) based on the computational hydrogen electrode model originally proposed by Nørskov and coworkers.[54,55]

$$\Delta G = \Delta E + \Delta E_{\mathrm{ZPE}} - T\Delta S + \Delta G_{\mathrm{pH}} + \Delta G_U \tag{12}$$

where ΔE is the difference in electronic energy before and after adsorption, and ΔE_{ZPE}, T, and ΔS represent the zero-point energy correction, temperature, and entropy change of the adsorption system, respectively. To compute the thermodynamic properties, the thermodynamic conditions were set to be 1 atmosphere and 298 K. The pH dependence of the reduction potential is given by $\Delta G_{\mathrm{pH}} = 0.059 \times \mathrm{pH}$, which stems from the dependence of the entropy on the H^+ concentration. ΔG_U is the contribution of the applied electrode potential (U) to ΔG.[56,57]

OER involves four electron steps, which can be written as step (1)–(4) oxidation reaction equations, as follows:

$$* + \mathrm{OH^-} \rightleftharpoons *\mathrm{OH} + \mathrm{e^-} \quad \text{(step 1)}$$

$$*\mathrm{OH} + \mathrm{OH^-} \rightleftharpoons *\mathrm{O} + \mathrm{H_2O} + \mathrm{e^-} \quad \text{(step 2)}$$

$$*\mathrm{O} + \mathrm{OH^-} \rightleftharpoons *\mathrm{OOH} + \mathrm{e^-} \quad \text{(step 3)}$$

$$*\mathrm{OOH} + \mathrm{OH^-} \rightleftharpoons * + \mathrm{O_2} + \mathrm{H_2O} + \mathrm{e^-} \quad \text{(step 4)}$$

Meanwhile, HER involves two-electron steps under alkaline conditions, which can be written as step (5)–(7) reduction reaction equations, as follows:

$$* + \mathrm{H_2O} + \mathrm{e^-} \rightleftharpoons *\mathrm{H_2O} \quad \text{(step 5)}$$

$$*\mathrm{H_2O} \rightleftharpoons *\mathrm{H} + \mathrm{OH^-} \quad \text{(step 6)}$$

$$*\mathrm{H} + \mathrm{H_2O} + \mathrm{e^-} \rightleftharpoons * + \mathrm{H_2} + \mathrm{OH^-} \quad \text{(step 7)}$$

where * denotes the adsorption site and *(radical) denotes the intermediate species adsorbed on the surface.

Considering the contribution from the zero-point energy, the entropy, the pH dependence of the redox potential, and the external potential supplied by the carrier, the free-energy changes along the reaction pathway for OER can be expressed as eqn (13)–(16).[58]

$$\Delta G_{*\mathrm{OH}} = G_{*\mathrm{OH}} + 1/2G_{\mathrm{H_2}} - G_{*} - G_{\mathrm{H_2O}} - \Delta G_{\mathrm{pH}} - eU \tag{13}$$

$$\Delta G_{*\mathrm{O}} = G_{*\mathrm{O}} + G_{\mathrm{H_2}} - G_{*} - G_{\mathrm{H_2O}} - 2\Delta G_{\mathrm{pH}} - 2eU \tag{14}$$

$$\Delta G_{*\mathrm{OOH}} = G_{*\mathrm{OOH}} + 3/2\mathrm{G_{H_2}} - G_{*} - 2G_{\mathrm{H_2O}} - 3\Delta G_{\mathrm{pH}} - 3eU \tag{15}$$

$$\Delta G_{*\mathrm{O_2}} = 2G_{\mathrm{H_2}} + G_{\mathrm{O_2}} - 2G_{*\mathrm{H_2O}} - 4\Delta G_{\mathrm{pH}} - 4eU \tag{16}$$

The free-energy changes along the reaction pathway for HER can be expressed as eqn (17)–(19).

$$\Delta G_{*\mathrm{H_2O}} = G_{*\mathrm{H_2O}} - G_{\mathrm{H_2O}} - G_{*} + \Delta G_{\mathrm{pH}} - eU \tag{17}$$

$$\Delta G_{*\mathrm{H}} = G_{*\mathrm{H}} - 1/2G_{\mathrm{H_2}} - G_{*} + \Delta G_{\mathrm{pH}} - eU \tag{18}$$

$$\Delta G_{*\mathrm{H_2}} = 2\Delta G_{\mathrm{pH}} - 2eU \tag{19}$$

Author contributions

Yang Liu: writing – original draft, methodology, investigation. Zhao-Di Yang: writing – review & editing, supervision, conceptualization. Rui Zhang: investigation. Yingchao Lai: investigation. Yu Zhang: writing – review & editing. Guiling Zhang: supervision, conceptualization.

Conflicts of interest

The authors declare no conflict of interest.

Data availability

The data that support the findings of this study are available from the corresponding author upon reasonable request.

Supplementary information (SI): figures of XRD patterns, FTIR spectra, XPS spectra, UV-vis spectrum, Mott–Schottky plots and bandgap, SEM, tables of ICP-OES. See DOI: https://doi.org/10.1039/d5im00302d.

Acknowledgements

This work was financially supported by the National Natural Science Foundation of China (Grant No. 52273288), the National Key R&D Program of China (Grant No. 2022YFC3901800), and the Heilongjiang Provincial Natural Science Foundation of China (Grant No. LH2024B016).

References

1 Y. Liu, Y. Chen, Y. Tian, T. Sakthivel, H. Liu, S. Guo, H. Zeng and Z. Dai, Synergizing hydrogen spillover and deprotonation by the internal polarization field in a MoS_2/$NiPS_3$ vertical heterostructure for boosted water electrolysis, *Adv. Mater.*, 2022, **34**, 2203615.

2 G. B. Liu, Y. S. Xu, T. Yang and L. H. Jiang, Recent advances in electrocatalysts for seawater splitting, *Nano Mater. Sci.*, 2023, **5**, 101–116.

3 Y. Wang, J. Li, P. J. Yang, H. D. Li, G. R. Xu, Y. M. Du, C. X. Li, W. Jin, T. Y. Ma, Z. X. Wu and L. Wang, Interfacial Ru nanoclusters in tandem with single atoms on oxygen-vacancy regulated CeO_2 for anion exchange membrane seawater-splitting, *J. Energy Chem.*, 2025, **102**, 618–627.

4 W. J. Liu, M. Zhou, J. W. Zhang, W. X. Liu, D. D. Qin, Q. Liu, G. Z. Hu and X. J. Liu, Construction of a CoP/MnP/Cu_3P heterojunction for efficient methanol oxidation-assisted seawater splitting, *Mater. Chem. Front.*, 2025, **9**, 953–964.

5 R. Wu, J. Xu, C.-L. Zhao, X.-Z. Su, Z.-L. Zhang, Y.-R. Zheng, F.-Y. Yang, X.-S. Zheng, J.-F. Zhu, J. Luo, W.-X. Li, M.-R. Gao and S.-H. Yu, Dopant triggered atomic configuration activates water splitting to hydrogen, *Nat. Commun.*, 2023, **14**, 2306.

6 Y. W. Gui, Z. T. Liu, X. B. Feng, Y. F. Jia, Y. M. Zhang, Y. M. Zhang, H. Y. Yang, Y. Zhang, M. Y. Li, L. Liang and J. W. Shi, One-step electrodeposition synthesis of NiFePS on carbon cloth as self-supported electrodes for electrochemical overall water splitting, *J. Colloid Interface Sci.*, 2024, **673**, 444–452.

7 M. S. Yang, J. Y. Ding, Z. W. Wang, J. W. Zhang, Z. M. Peng and X. J. Liu, NiMo-based alloy and its sulfides for energy-saving hydrogen production via sulfion oxidation assisted alkaline seawater splitting, *Chin. Chem. Lett.*, 2025, **36**, 110861.

8 Z. S. Li, B. L. Li, M. Yu, C. L. Yu and P. K. Shen, Amorphous metallic ultrathin nanostructures: a latent ultra-high-density atomic-level catalyst for electrochemical energy conversion, *Int. J. Hydrogen Energy*, 2022, **47**, 26956–26977.

9 K. Song, H. Zhang, Z. Lin, Z. Wang, L. Zhang, X. Shi, S. Shen, S. Chen and W. Zhong, Interfacial engineering of cobalt thiophosphate with strain effect and modulated electron structure for boosting electrocatalytic hydrogen evolution reaction, *Adv. Funct. Mater.*, 2024, **34**, 2312672.

10 R. Yin, Z. Wang, J. Zhang, W. Liu, J. He, G. Hu and X. Liu, Tunable NiSe-Ni_3Se_2 heterojunction for energy-efficient hydrogen production by coupling urea degradation, *Small Methods*, 2025, **9**, 2401976.

11 D. Sui, R. S. Luo, S. M. Xie, H. Zhang, T. T. Ma, H. Sun, T.-T. Jia, J. Sun and X. Y. Li, Atomic ruthenium doping in collaboration with oxygen vacancy engineering boosts the hydrogen evolution reaction by optimizing H absorption, *Chem. Eng. J.*, 2024, **480**, 148007.

12 J. N. Hansen, H. Prats, K. K. Toudahl, N. M. Secher, K. Chan, J. Kibsgaard and I. Chorkendorff, Is there anything better than Pt for HER?, *ACS Energy Lett.*, 2021, **6**, 1175.

13 X. Chen, X.-T. Wang, J.-B. Le, S.-M. Li, X. Wang, Y.-J. Zhang, P. Radjenovic, Y. Zhao, Y.-H. Wang, X.-M. Lin, J.-C. Dong and J.-F. Li, Revealing the role of interfacial water and key intermediates at ruthenium surfaces in the alkaline hydrogen evolution reaction, *Nat. Commun.*, 2023, **14**, 5289.

14 Q. He, Y. Zhou, H. Shou, X. Wang, P. Zhang, W. Xu, S. Qiao, C. Wu, H. Liu, D. Liu, S. Chen, R. Long, Z. Qi, X. Wu and L. Song, Synergic reaction kinetics over adjacent ruthenium sites for superb hydrogen generation in alkaline media, *Adv. Mater.*, 2022, **34**, 2110604.

15 Y. Zheng, Y. Jiao, A. Vasileff and S.-Z. Qiao, The hydrogen evolution reaction in alkaline solution: From theory, single crystal models, to practical electrocatalysts, *Angew. Chem., Int. Ed.*, 2018, **57**, 7568.

16 H. Zhao, D. Chen, R. Yu, J. Jiao, W. Zeng, J. Zhu, X. Mu, Y. Yao, D. Wu, Y. Zhang, J. Wu and S. Mu, Atomizing platinum for hydrogen electrode reactions, *Nano Energy*, 2024, **121**, 109247.

17 X. A. Teng, Z. B. Wang, Y. S. Wu, Y. Zhang, B. Yuan, Y. Y. Xu, R. M. Wang and A. X. Shan, Enhanced alkaline hydrogen evolution reaction of MoO_2/Ni_3S_2 nanorod arrays by interface engineering, *Nano Energy*, 2024, **122**, 109299.

18 H. Ren, Z. Zhang, Z. Geng, Z. Wang, F. Shen, X. Liang, Z. Cai, Y. Wang, D. Cheng, Y. Cao, X. Yang, M. Hu, X. Yao and K. Zhou, Gradient OH desorption facilitating alkaline hydrogen evolution over ultrafine quinary nanoalloy, *Adv. Energy Mater.*, 2024, **14**, 2400777.

19 Y.-N. Zhou, W.-L. Yu, H.-J. Liu, R.-Y. Fan, G.-Q. Han, B. Dong and Y.-M. Chai, Self-integration exactly constructing oxygen-modified MoNi alloys for efficient hydrogen evolution, *EcoEnergy*, 2023, **1**, 425–436.

20 J. J. Yan, Y. Chang, J. X. Chen, M. L. Jia and J. C. Jia, Understanding the copper-iridium nanocrystals as highly effective bifunctional pH-universal electrocatalysts for water splitting, *J. Colloid Interface Sci.*, 2023, **642**, 779–788.

21 Y. Chen, Y. D. Liu, W. F. Zhai, H. Liu, T. Sakthivel, S. W. Guo and Z. F. Dai, Metastabilizing the ruthenium clusters by

interfacial oxygen vacancies for boosted water splitting electrocatalysis, *Adv. Energy Mater.*, 2024, **14**, 2400059.

22 S. Anantharaj, S. Kundu and S. Noda, "The Fe effect": A review unveiling the critical roles of Fe in enhancing OER activity of Ni and Co based catalysts, *Nano Energy*, 2021, **80**, 105514.

23 C. Li, H. Zhang, M. Liu, F.-F. Lang, J. D. Pang and X.-H. Bu, Recent progress in metal-organic frameworks (MOFs) for electrocatalysis, *Ind. Chem. Mater.*, 2023, **1**, 9–38.

24 Z. Di, C. Liu, J. Pang, C. Chen, F. Hu, D. Yuan, M. Wu and M. Hong, Cage-like porous materials with simultaneous high C_2H_2 storage and excellent C_2H_2/CO_2 separation performance, *Angew. Chem., Int. Ed.*, 2021, **60**, 10828–10832.

25 L. Kong, M. Liu, H. Huang, Y. Xu and X.-H. Bu, Metal/covalent-organic framework based cathodes for metal-ion batteries, *Adv. Energy Mater.*, 2022, **12**, 2100172.

26 B. Geng, F. Yan, X. Zhang, Y. He, C. Zhu, S.-L. Chou, X. Zhang and Y. Chen, Conductive CuCo-based bimetal organic framework for efficient hydrogen evolution, *Adv. Mater.*, 2021, **33**, e2106781.

27 Z. Qiu, Y. Li, Y. Gao, Z. Meng, Y. Sun, Y. Bai, N.-T. Suen, H.-C. Chen, Y. Pi and H. Pang, 2D MOF-assisted pyrolysis-displacement-alloying synthesis of high-entropy alloy nanoparticles library for efficient electrocatalytic hydrogen oxidation, *Angew. Chem., Int. Ed.*, 2023, **62**, e202306881.

28 Q. N. Liang, J. M. Chen, F. L. Wang and Y. W. Li, Transition metal-based metal-organic frameworks for oxygen evolution reaction, *Coord. Chem. Rev.*, 2020, **424**, 213488.

29 Y. K. Song, W. F. Xie, M. F. Shao and X. Duan, Integrated electrocatalysts derived from metal organic frameworks for gas-involved reactions, *Nano Mater. Sci.*, 2023, **5**, 161–176.

30 Y. S. Wei, M. Zhang, M. Kitta, Z. Liu, S. Horike and Q. Xu, A single-crystal open-capsule metal-organic framework, *J. Am. Chem. Soc.*, 2019, **141**, 7906–7916.

31 J. W. Li, P. Liu, J. X. Mao, J. X. Yan and W. B. Song, Two-dimensional conductive metal-organic frameworks with dual metal sites toward the electrochemical oxygen evolution reaction, *J. Mater. Chem. A*, 2021, **9**, 1623–1629.

32 Y. Lian, W. Yang, C. Zhang, H. Sun, Z. Deng, W. Xu, L. Song, Z. Ouyang, Z. Wang, J. Guo and Y. Peng, Unpaired 3d electrons on atomically dispersed cobalt centres in coordination polymers regulate both oxygen reduction reaction (ORR) activity and selectivity for use in zinc-air batteries, *Angew. Chem., Int. Ed.*, 2020, **59**, 286–294.

33 D. N. Xing, Y. Y. Wang, P. Zhou, Y. Y. Liu, Z. Y. Wang, P. Wang, Z. K. Zheng, H. F. Cheng, Y. Dai and B. B. Huang, Co_3(hexaiminotriphenylene)$_2$: A conductive two-dimensional π-d conjugated metal-organic framework for highly efficient oxygen evolution reaction, *Appl. Catal., B*, 2020, **278**, 119295.

34 J. Park, A. C. Hinckley, Z. H. Huang, D. W. Feng, A. A. Yakovenko, M. Lee, S. C. Chen, X. D. Zou and Z. N. Bao, Synthetic routes for a 2D semiconductive copper hexahydroxybenzene metal-organic framework, *J. Am. Chem. Soc.*, 2018, **140**, 14533–14537.

35 Q. Jiang, P. Xiong, J. Liu, Z. Xie, Q. Wang, X.-Q. Yang, E. Hu, Y. Cao, J. Sun, Y. Xu and L. Chen, A redox-active 2D metal-organic framework for efficient lithium storage with extraordinary high capacity, *Angew. Chem., Int. Ed.*, 2020, **59**, 5273–5277.

36 Z. Guo, S. Yang, M. Liu, Q. Xu and G. Zeng, Construction of core-shelled covalent/metal-organic frameworks for oxygen evolution reaction, *Small*, 2024, **20**, 2308598.

37 M. H. Liu, Q. Xu, Q. Y. Miao, S. Yang, P. Wu, G. J. Liu, J. He, C. B. Yu and G. F. Zeng, Atomic Co-N_4 and Co nanoparticles confined in COF@ZIF-67 derived core-shell carbon frameworks: Bifunctional non-precious metal catalysts toward the ORR and HER, *J. Mater. Chem. A*, 2022, **10**, 228–233.

38 G. F. Li, D. Wang, Q. Xing, G. Zhou, S. Liu, Y. Li, L. Zheng, P. Ye and J. Zou, Design and syntheses of MOF/COF hybrid materials via postsynthetic covalent modification: An efficient strategy to boost the visible-light-driven photocatalytic performance, *Appl. Catal., B*, 2019, **243**, 621–628.

39 H. Peng, J. Raya, F. Richard, W. Baaziz, O. Ersen, A. Ciesielski and P. Samori, Synthesis of robust MOFs@COFs porous hybrid materials via an Aza-Diels-Alder reaction: Towards high-performance supercapacitor materials, *Angew. Chem., Int. Ed.*, 2020, **59**, 19602–19609.

40 S. Zhou, Y. Kuang, H. Yang, L. Gan, X. Feng, C. Mao, L. Chen, J. Zheng and G. Ouyang, Structure-controlled interpenetrated MOF@COF via C-C linkage for enhanced photocatalysis, *Angew. Chem., Int. Ed.*, 2024, **62**, e202412279.

41 J. H. Li, P. X. Liu, Y. Chen, J. F. Zhou, J. W. Li, J. F. Yang, D. L. Zhang, J. P. Li and L. B. Li, A customized hydrophobic porous shell for MOF-5, *J. Am. Chem. Soc.*, 2023, **145**, 19707–19714.

42 M. Gao, M. Qi, L. Liu and Z. Han, An exceptionally stable core-shell MOF/COF bifunctional catalyst for a highly efficient cascade deacetalization-Knoevenagel condensation reaction, *Chem. Commun.*, 2019, **55**, 6377–6380.

43 C. H. Yang, Z.-D. Yang, H. Dong, N. Sun, Y. Lu, F.-M. Zhang and G. L. Zhang, Theory-driven design and targeting synthesis of a highly-conjugated basal-plane 2D covalent organic framework for metal-free electrocatalytic OER, *ACS Energy Lett.*, 2019, **4**, 2251–2258.

44 L. Zhao, J. Yan, H. Huang, X. Du, H. Chen, X. He, W. Li, W. Fang, D. Wang, X. Zeng, J. Dong and Y. Liu, Regulating electronic structure of bimetallic NiFe-THQ conductive metal-organic frameworks to boost catalytic activity for oxygen evolution reaction, *Adv. Funct. Mater.*, 2024, **34**, 2310902.

45 J. Zhao, Y. Zhang, H. Lu, Y. Wang, X. D. Liu, M. K. S. Hirbod, J. Peng, S. Chen, X. Li and Y. Zhang, Additive manufacturing of two-dimensional conductive metal-organic framework with multidimensional hybrid architectures for high-performance energy storage, *Nano Lett.*, 2022, **22**, 1198–1206.

46 G. Chen, L. B. Gee, W. Xu, Y. Zhu, J. S. Lezama-Pacheco, Z. Huang, Z. Li, J. T. Babicz, S. Choudhury, T.-H. Chang, E. Reed, E. I. Solomon and Z. Bao, Valence-dependent electrical conductivity in a 3D tetrahydroxyquinone-based metal-

organic framework, *J. Am. Chem. Soc.*, 2020, **142**, 21243–21248.

47 J. M. Wei, M. Zhou, A. C. Long, Y. M. Xue, H. B. Liao, C. Wei and Z. C. J. Xu, Heterostructured electrocatalysts for hydrogen evolution reaction under alkaline conditions, *Nano-Micro Lett.*, 2018, **10**, 75.

48 J. Zhu, L. S. Hu, P. X. Zhao, L. Y. S. Lee and K.-Y. Wong, Recent advances in electrocatalytic hydrogen evolution using nanoparticles, *Chem. Rev.*, 2020, **120**, 851–918.

49 M. Cabán-Acevedo, M. L. Stone, J. R. Schmidt, J. G. Thomas, Q. Ding, H.-C. Chang, M.-L. Tsai, J.-H. He and S. Jin, Efficient hydrogen evolution catalysis using ternary pyrite-type cobalt phosphosulphide, *Nat. Mater.*, 2015, **14**, 1245–1251.

50 J. Q. Tian, Q. Liu, A. M. Asiri and X. P. Sun, Self-supported nanoporous cobalt phosphide nanowire arrays: An efficient 3D hydrogen-evolving cathode over the wide range of pH 0-14, *J. Am. Chem. Soc.*, 2014, **136**, 7587–7590.

51 G. Kresse and J. Hafner, Ab initio molecular dynamics for liquid metals, *Phys. Rev. B*, 1993, **47**, 558.

52 G. Kresse and J. Hafner, Ab initio molecular-dynamics simulation of the liquid-metal-amorphous-semiconductor transition in germanium, *Phys. Rev. B: Condens. Matter Mater. Phys.*, 1994, **49**, 14251.

53 P. E. Blöchl, Projector augmented-wave method, *Phys. Rev. B: Condens. Matter Mater. Phys.*, 1994, **50**, 17953.

54 J. G. Howalt, T. Bligaard, J. Rossmeisl and T. Vegge, DFT based study of transition metal nano-clusters for electrochemical NH_3 production, *Phys. Chem. Chem. Phys.*, 2013, **15**, 7785–7795.

55 J. K. Nørskov, J. Rossmeisl, A. Logadottir, L. Lindqvist, J. R. Kitchin, T. Bligaard and H. Jónsson, Origin of the overpotential for oxygen reduction at a fuel-cell cathode, *J. Phys. Chem. B*, 2004, **108**, 17886–17892.

56 A. A. Peterson, F. A. Pedersen, F. Studt, J. Rossmeisl and J. K. Nørskov, How copper catalyzes the electroreduction of carbon dioxide into hydrocarbon fuels, *Energy Environ. Sci.*, 2010, **3**, 1311–1315.

57 G. Ertl, S. B. Lee and M. Weiss, Kinetics of nitrogen adsorption on Fe(111), *Surf. Sci.*, 1982, **114**, 515–526.

58 Y. Y. Wan, L. Wang, H. X. Xu, X. J. Wu and J. L. Yang, A simple molecular design strategy for two-dimensional covalent organic framework capable of visible-light-driven water splitting, *J. Am. Chem. Soc.*, 2020, **142**, 4508–4516.